Research Article Vol. 33, No. 1 / 13 Jan 2025 / Optics Express 1556
Optics EXPRESS

Tailoring second harmonic generation in a multilayer WS_2 flake via a silicon circular Bragg grating

LIN CAI,[1,†] YUHENG MAO,[1,†] LIDAN ZHOU,[2] JINSHAN LUO,[1] SHIMEI LIU,[1] SHULEI LI,[3] FU DENG,[1,4] AND SHENG LAN[1,5]

[1]*Guangdong Provincial Key Laboratory of Nanophotonic Functional Materials and Devices, School of Optoelectronic Science and Engineering, South China Normal University, Guangzhou 510006, China*
[2]*State Key Laboratory of Optoelectronic Materials and Technologies and School of Electronics and Information Technology, Sun Yat-Sen University, Guangzhou 51006, China*
[3]*School of Optoelectronic Engineering, Guangdong Polytechnic Normal University, Guangzhou 510665, China*
[4]*fu_deng@foxmail.com*
[5]*slan@scnu.edu.cn*
[†]These authors contributed equally to this work

Abstract: Nonlinear emission phenomena observed in transition metal dichalcogenides (TMDCs) have significantly advanced the development of robust nonlinear optical sources within two-dimensional materials. However, the intrinsic emission characteristics of TMDCs are inherently dependent on the specific material, which constrains their tunability for practical applications. In this study, we propose a strategy for the selective enhancement and modification of second-harmonic generation (SHG) emission in a multilayer WS_2 flake through the implementation of a silicon (Si)-based circular Bragg grating (CBG) structure positioned on an Au/SiO_2 substrate. By selectively exciting the region of the circular Bragg grating with the grating oriented either parallel or perpendicular to the linearly polarized pump beam, we successfully achieved wavelength-tunable SHG intensity peaks at 402.5 nm and 425 nm for the respective alignments. Our experimental findings, corroborated by numerical simulations, indicate that the enhancement of SHG intensity is highly sensitive to the orientation of the grating region of the CBG. Power-dependent SHG spectra further validate the quadratic dependence of SHG, while comparative analysis with WS_2 flakes on a bare $Si/Au/SiO_2$ substrate highlights the critical role of the CBG structure in modulating SHG. This research underscores the potential of CBG-augmented TMDCs for the control of nonlinear optical emissions, suggesting promising applications in photonic devices and selective emission technologies.

1. Introduction

The investigation of two-dimensional (2D) materials has attracted considerable scholarly interest in recent years [1], primarily due to their distinctive optical and electronic properties that set them apart from their bulk equivalents [2]. These materials, which typically consist of only a few atomic layers [3], demonstrate exceptional attributes such as a high surface area, mechanical flexibility, and outstanding electronic and optical properties [4]. Among the diverse array of 2D materials, TMDCs have emerged as significant candidates for applications in various domains, including electronics, photonics, and energy storage [3]. A particularly intriguing feature of TMDCs is their nonlinear optical behavior, which arises from their unique crystal structures and symmetry characteristics [5–7]. Specifically, SHG has emerged as a potent technique for probing the symmetry and electronic structure of these materials [8–10]. In the SHG process, two photons interact to produce a new photon with double the energy (and consequently half the wavelength) of the incident light [11]. This property renders SHG especially valuable for

#547760 https://doi.org/10.1364/OE.547760
Journal © 2025 Received 11 Nov 2024; revised 22 Dec 2024; accepted 23 Dec 2024; published 10 Jan 2025

Optics EXPRESS

characterizing materials that lack inversion symmetry [12]. Enhancing SHG in TMDCs is crucial for advancing applications in photonics, optoelectronics, and quantum information technologies, thereby facilitating the development of efficient light sources and detectors that leverage the exceptional properties of these 2D materials [13].

Despite the inherent nonlinear optical characteristics of multilayer TMDCs, the efficiency of SHG emission can be limited by several factors, including material thickness [14], layer stacking [9], and the local environment surrounding the material [15–17]. For instance, variations in the number of layers can significantly affect the material's symmetry [12], thereby influencing its nonlinear optical response. Additionally, the effects of optical confinement and enhancement can be influenced by the substrate and overall device architecture [16]. To address these challenges, researchers have explored various strategies to enhance SHG, including the utilization of structured substrates designed to optimize light-matter interactions [18,19]. Notably, self-forming cavities that utilize multilayer MoS_2 on thin metal films (such as Au or silver) have demonstrated substantial enhancements in SHG emission [15]. Furthermore, optical resonances in patterned TMDC nanostructures have proven effective in augmenting SHG for multilayer TMDC structures [20–24], providing a novel avenue for investigating TMDC-based nonlinear phenomena [13,25].

Another promising strategy involves the use of external optical cavities through meta-structures to amplify SHG intensity in layered TMDCs [26,27], thereby opening new pathways for exploring the nonlinear properties of these materials. Dielectric CBGs, in particular, have shown significant potential in manipulating light-matter interactions through engineered photonic structures [28–30]. These gratings are specifically designed to create resonant conditions that enhance the electric field in localized regions, leading to improved SHG emission from the underlying material [30]. By meticulously adjusting the geometrical parameters of the CBGs, such as their period and depth, researchers can precisely control the wavelength and directionality of the emitted light, paving the way for advanced applications in integrated photonics [31]. While previous studies have successfully demonstrated the use of CBGs to enhance photoluminescence and SHG in monolayer TMDCs [27,32,33], there remains a notable gap in the literature regarding the effects of CBGs on multilayer TMDC flakes. This gap presents a unique opportunity to investigate how a CBG structure can modify the nonlinear emission characteristics of multilayer TMDC flakes.

In this study, we demonstrate the selective enhancement and modification of SHG from a multilayer WS_2 flake positioned atop a Si-CBG structure on an Au/SiO_2 substrate. Our research aims to elucidate how the geometry and orientation of the selective region of the CBG significantly influence the SHG emission characteristics of the multilayer WS_2 flake. By employing a combination of numerical simulations and experimental measurements, we analyze the electric field distributions and enhancement factors that contribute to the observed enhancements in SHG intensity and wavelength selectivity. This comprehensive approach enables us to elucidate the underlying mechanisms driving SHG modulation in multilayer TMDCs, providing valuable insights into the design of photonic structures optimized for nonlinear optical performance. Our findings not only address critical aspects of SHG enhancement in multilayer WS_2 but also underscore the importance of external engineering in the pursuit of efficient nonlinear optical devices. Furthermore, this work may inspire future research into the integration of TMDCs with advanced photonic platforms, facilitating the realization of sophisticated functionalities, including integrated light sources, efficient photodetectors, and nonlinear optical devices for signal processing.

2. Materials and methods

2.1. Sample preparation and characterization

For the sample fabrication, a crystalline Si (c-Si) film was successfully transferred from a silicon-on-insulator (SOI) wafer to a quartz substrate through a process that integrates adhesive wafer bonding with chemical polishing, adhering to methodologies established in previous research

Optics EXPRESS

[34]. The preparation of the SOI wafer involved the deposition of a 50 nm Au layer, followed by a 15 nm SiO_2 layer, onto a 220 nm c-Si film supported by a 2 µm-thick SiO_2 layer. Subsequently, an ultraviolet-curable adhesive (NOA61) was applied to the SOI wafer via spin-coating, which was then bonded to a quartz substrate. The silicon substrate was selectively removed through a combination of chemical polishing and dry etching techniques. The final transfer of the c-Si film to the quartz substrate was achieved by dissolving the SiO_2 layer of the SOI with hydrofluoric acid (HF). The patterning process for the silicon CBG was executed using electron-beam lithography and dry etching techniques. Initially, a 400 nm layer of resist (ARP6200.09) was spin-coated onto the sample for electron-beam lithography, which was conducted using an EBPG5000Plus system (Raith) at an accelerating voltage of 100 kV. The exposed resist was developed in xylene, and the pattern was subsequently transferred to the c-Si layer using an inductively coupled plasma (ICP) tool (Oxford Instruments). The morphology of the resulting silicon nanopillars was characterized by using scanning electron microscopy (SEM) (Auriga, Zeiss), as detailed in the following sections. Finally, multilayer WS_2 flakes were mechanically exfoliated from bulk crystals onto polydimethylsiloxane (PDMS) stamps utilizing the Scotch-tape method and were then transferred onto the well-prepared CBG/ Au/SiO_2 structure using an all-dry-transfer method.

2.2. Optical characterization

The optical properties of the hybrid multilayer WS_2 flake situated on the CBG/Au/SiO_2 substrate were investigated utilizing an inverted microscope (Observer A1, Zeiss) equipped with both white light and femtosecond laser excitation sources. A femtosecond laser (Mira 900S, Coherent; pulse duration of 130 fs and repetition rate of 76 MHz) was employed to excite the multilayer WS_2 flake on the CBG/Au/SiO_2 structure via focusing with a 40× objective lens, with polarization controlled by a custom-built polarizer. The resultant SHG emissions from the WS_2 flake were collected through the same objective lens and subsequently directed either to a spectrometer (SR-500i-B1, Andor) for spectral analysis or to charge-coupled devices (DU970N, Andor) for imaging purposes. SHG signal mapping across the hybrid multilayer WS_2 flake on the CBG/Au/SiO_2 structure was conducted using a confocal laser scanning microscope (A1MP, Nikon).

2.3. Numerical simulation

The enhancement of the electric field in a multilayer WS_2 flake situated on a CBG/Au/SiO_2 film structure was modeled using the finite-difference time-domain (FDTD) method, specifically through the application of Lumerical FDTD Solutions software. In this simulation, the multilayer WS_2 flake was characterized as a planar structure with a thickness ranging from 60 to 70 nm, with its refractive index parameters obtained from the relevant literature [35]. The dimensions of the Si CBG structure were adjusted according to experimental measurements derived from SEM images, with the layer thicknesses set at 220 nm for the CBG structure, 50 nm for the gold film, and 5 nm for the SiO_2 layer. The dielectric constants for Au and Si were referenced from the literature [36,37], while the refractive index for SiO_2 was assigned a value of 1.45. A self-adaptive mesh was utilized throughout the entire structure to ensure high precision, and perfectly matched layers (PML) conditions were implemented in all directions to effectively confine the simulation domain.

3. Results and discussion

Figure 1(a) shows a schematic representation of the modification of SHG emission from a multilayer WS_2 flake positioned on a Si CBG structure over an Au/SiO_2 substrate. The incorporation of a thin Au film within the structure enhances the reflection of waves from the substrate, thereby amplifying the experimental signal. The Si-based CBG structure, which has been meticulously fabricated using EBL and RIE, is illustrated in the SEM image inset in Fig. 1(a). The dimensions of the CBG are specified as follows: the width of the ring is 100

Optics EXPRESS

nm, the inter-ring distance is also 100 nm, and the radius of the central disk is approximately 80 nm, as shown in the lower left section of Fig. 1(a). Furthermore, the multilayer WS_2 flakes were mechanically exfoliated from bulk crystals and subsequently transferred onto the precisely prepared CBG/Au/SiO_2 structure using an all-dry-transfer method. Given that the dimensions of the CBG are approximately 10 μm—substantially larger than the pump laser spot size of approximately 1 μm—SHG emission from the multilayer WS_2 flake can be selectively observed at various locations on the CBG structure. For the linearly polarized pump beam, the CBG structure is categorized into two distinct regions: one aligned with the polarization direction and the other oriented perpendicularly. This configuration facilitates the selective enhancement of SHG emission from the multilayer WS_2 flake, driven by the CBG structure. The corresponding SHG spectra for the WS_2 flake in both the parallel and perpendicular regions are presented in Fig. 1(b). For comparative purposes, the SHG spectrum of the WS_2 flake positioned directly on the Au film, absent the CBG structure, is represented as a gray line. Notably, the presence of the CBG structure increases the SHG intensity by approximately fivefold in both configurations compared to the scenario without the CBG. Additionally, the wavelength of maximum SHG enhancement is influenced by the orientation of the CBG grating relative to the pump beam polarization; specifically, enhancement is observed at 402.5 nm for the grating aligned with the polarization and shifts to 425 nm for the perpendicular orientation.

Figure 1(c) provides a detailed examination of the WS_2 flake situated atop the CBG on the Au/SiO_2 substrate, with the CBG structure delineated by circles. The multilayer WS_2 flake was acquired through mechanical exfoliation from bulk WS_2 crystal and subsequently transferred onto the CBG structure, as elaborated in our previous research [15,16]. The optical image corroborates the successful transfer of the multilayer WS_2 flake onto the CBG, indicating that two CBG structures are indeed covered by the WS_2 flake, as highlighted by the red and green circles. The variation in colors within the multilayer WS_2 flakes corresponds to differences in layer thickness, a characteristic commonly observed in mechanically exfoliated TMDCs. Notably, the flake in the lower left region appears thicker than that in the upper right, which significantly affects the modification of SHG emission, as demonstrated by the SHG mapping obtained through two-photon microscopy in Figs. 1(d)-(g). In the lower left region, the SHG emission mappings indicate that the emission pattern is influenced by the polarization of the pump beam, with enhanced SHG occurring where the underlying CBG structure is aligned parallel to the pump beam polarization for both x (Fig. 1(d)) and y (Fig. 1(e)) orientations. It is essential to note that the SHG mapping is not uniform across the entire WS_2 flake on the CBG structure, due to minor variations in layer thickness of WS_2 flake from mechanical exfoliation. The centrosymmetric structure of even-numbered H-phase TMDCs suppresses SHG emission, as discussed in previous studies [12,14]. The white dashed lines in Figs. 1(d) and (e) represent the boundaries between different layers of the WS_2 flake, accounting for the dark regions observed even above the CBG structure. For comparative purposes, Figs. 1(f) and 1 g illustrate another area of the thinner WS_2 flake on the CBG structure, where the modification of SHG emission is notably weaker than in the thicker WS_2 flake depicted in Figs. 1(d) and 1(e). Consequently, our focus will remain on the regions marked by dashed lines to further investigate the modification of SHG emission in the WS_2 flake attributable to the CBG structure in subsequent discussions.

To elucidate the mechanism underlying the selective enhancement of SHG emission in the multilayer WS_2 flake facilitated by the CBG structure, we performed numerical simulations utilizing the FDTD method. These simulations were employed to calculate the electric field distribution and enhancement within the WS_2 flake positioned atop the CBG grating. In our modeling, the WS_2 flake was represented as a planar structure with variable thickness to accurately reflect the experimental layer distribution, as illustrated in Fig. 2(a). Two specific regions of the CBG structure-aligned both parallel and perpendicular to the linearly polarized pump beam-are indicated by yellow arrows. To correspond with the SHG emission spectra observed for the

Optics EXPRESS

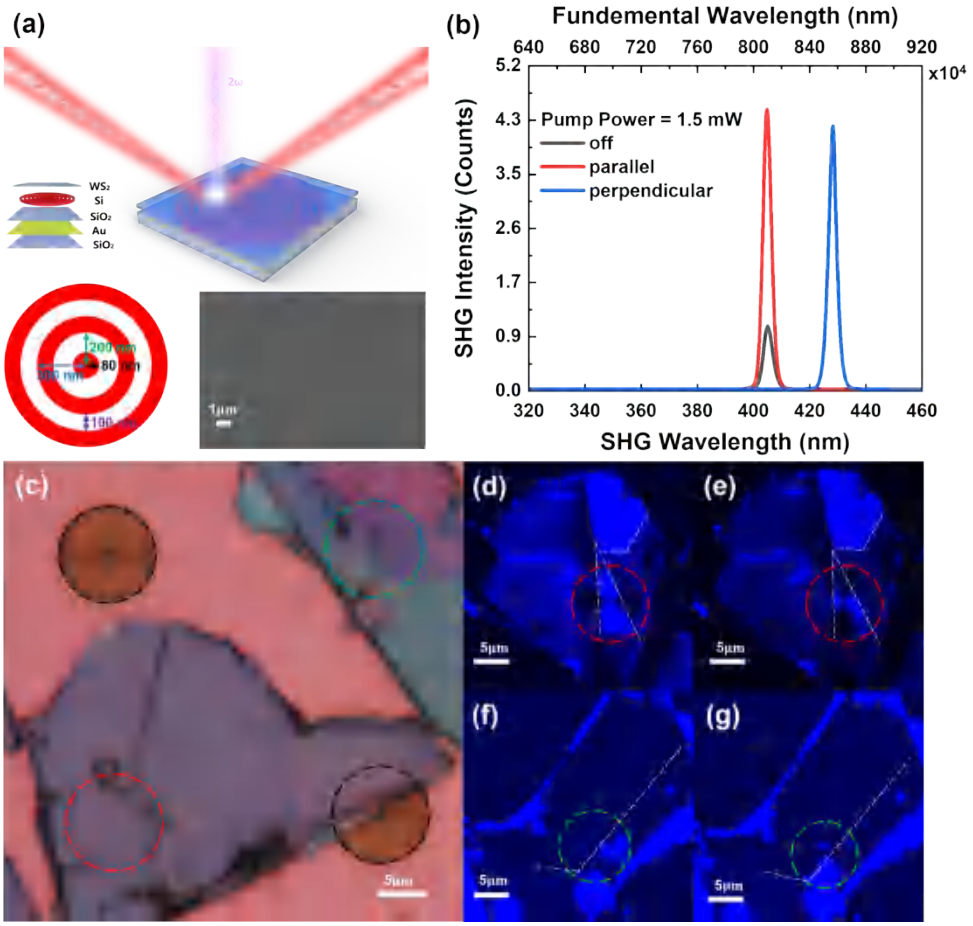

Fig. 1. (a) Schematic of SHG emission from a multilayer WS_2 flake positioned on a Si CBG/Au/SiO_2 structure and illuminated by a femtosecond laser. The insets in the lower panels show the parameters and an SEM image of the CBG structure used in the experiment. (b) SHG spectra of the multilayer WS_2 at three regions: without the CBG/Au/SiO_2 structure (gray), with grating direction parallel to the pump beam polarization (red), and with grating direction perpendicular to the pump beam polarization (blue). The measurement was conducted with a pump power of 1.5 mW. (c) Optical image of the multilayer WS_2 flake on the CBG/Au/SiO_2 structure, with circles indicating the CBG structure locations. The red circle indicates the CBG/Au/SiO_2 structure located beneath the WS_2 flake, as referenced in panels (d) and (e). The green circle highlights a similar structure corresponding to panels (f) and (g), whereas the black circles represent CBGs that are not completely covered by WS_2. (d), (e) SHG intensity mappings of the WS_2 flake on the CBG/Au/SiO_2 structure under x-polarized (d) and y-polarized (e) pump laser excitation. White dashed lines indicate regions of differing WS_2 flake thickness. (f), (g) SHG mappings for a different region of the multilayer WS_2 flake on the CBG/Au/SiO_2 structure, captured under identical conditions as in (d) and (e), for comparison.

multilayer WS_2 flake on the CBG structure, a Gaussian beam with a numerical aperture (NA) of 0.6 was focused on the vertical center of the CBG structure to induce excitation. Given the variability in thickness of the multilayer WS_2 flake resulting from mechanical exfoliation, this simulation accommodates random layer thickness. For the calculation of the SHG emission

Optics EXPRESS

enhancement factor, we employed a standard approach that integrates the fourth power of the electric field over the area of the WS_2 flake. This methodology effectively illustrates the two-photon absorption process I^2 that drives both SHG and two-photon photoluminescence [38,39], as represented by the following equation:

$$I^2 = \frac{1}{V}\int |E_{WS_2}/E_0|^4 dV$$

where $|E_{WS_2}/E_0|$ represents the electric field enhancement within the multilayer WS_2 flake, and V is the volume of the WS_2 flake situated on top of the CBG structure.

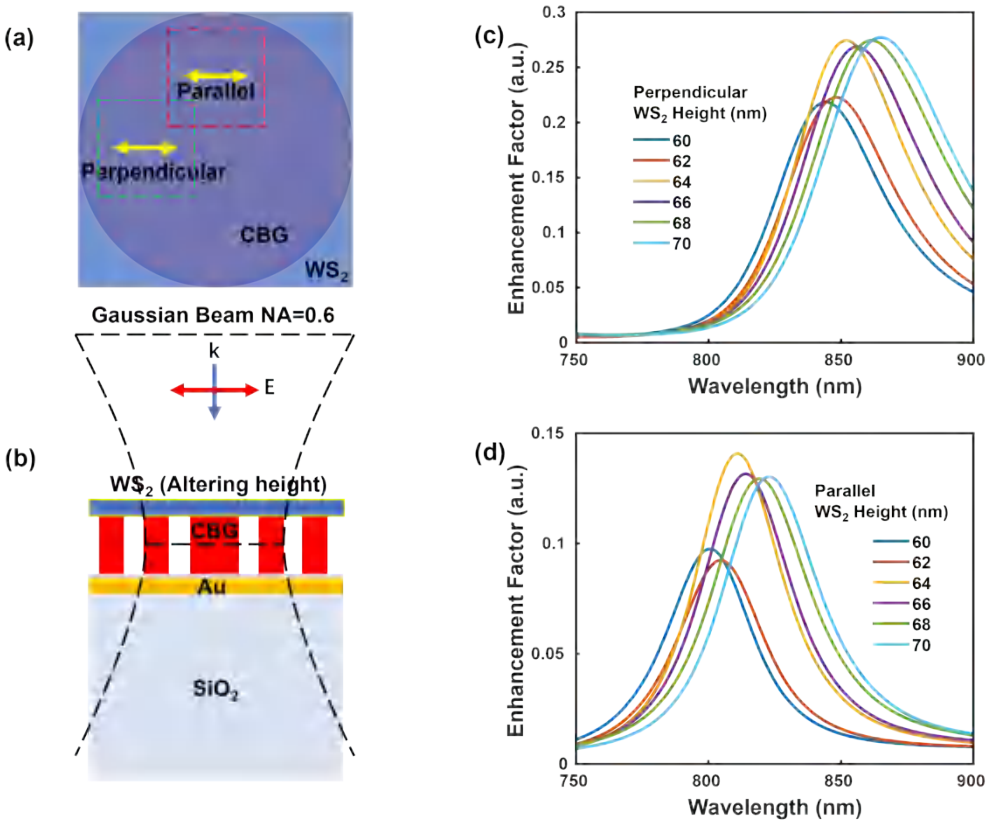

Fig. 2. Simulated electric field enhancement factor of the hybrid multilayer WS_2-CBG/Au/SiO_2 structure. (a) Schematic of the multilayer WS_2 on CBG/Au/SiO_2 structure, showing selective excitation regions where the grating is either parallel (red rectangular outlined region) or perpendicular (green rectangular outlined region) to the pump beam's polarization. (b) Illustration of the multilayer WS_2-CBG/Au/SiO_2 structure under Gaussian beam illumination in the simulation, with a numerical aperture (NA) of 0.6 focused at the CBG structure's center. (c), (d) Wavelength-dependent electric field enhancement factor for the multilayer WS_2-CBG/Au/SiO_2 structure at regions with the grating direction perpendicular (c) and parallel (d) to the polarization of the incident beam, with varying WS_2 layer thickness.

The wavelength-dependent electric field enhancement factors for regions aligned both parallel and perpendicular to the incident beam are illustrated in Figs. 2(c) and 2(d). These factors were calculated for a WS_2 flake thickness ranging from 60 to 70 nm, as determined through optical imaging conducted during the experiment. In the region where the grating is oriented

Optics EXPRESS

perpendicular to the polarization of the pump beam, the enhancement factor reaches its maximum near 850 nm, and this peak can be adjusted by varying the thickness of the WS_2 flake. The enhancement factor increases with WS_2 thickness beyond 64 nm and stabilizes for thicker layers. Conversely, in the region where the grating direction is aligned parallel to the polarization of the pump beam, the electric field enhancement factor peaks around 805 nm. Notably, similar to the perpendicular orientation, the enhancement factor also increases with WS_2 thickness beyond 64 nm. Consequently, the wavelength-selective SHG enhancement observed in the multilayer WS_2 flake, as noted across different regions of the CBG structure (Fig. 1(b)), can be qualitatively elucidated by the wavelength-specific electric field enhancement. This selective electric field enhancement presents a novel strategy for optimizing nonlinear emission in multilayer TMDC flakes.

After understanding the mechanism underlying the selective enhancement of SHG emission in the WS_2 flake on the CBG structure, we will explore the insights regarding directional emission derived from the SHG mapping presented in Figs. 1(d) and 1(e), which are informed by numerical simulations. In this context, a linearly polarized plane wave is employed as the excitation source to replicate the experimental mapping results. Figure 3(a) depicts a lateral view of the hybrid structure utilized in the simulation, which includes an electric field detector positioned at the center of the WS_2 flake. To accommodate the variations in thickness of the WS_2 flake resulting from mechanical exfoliation, the simulation permits adjustments to the flake thickness to align with the experimental outcomes. Specifically, we present electric field distributions for WS_2 flake thicknesses of 60 nm (illustrated in Figs. 3(b) and 3(c)) and 30 nm (shown in Figs. 3(d) and 3(e)) atop the CBG structure. The fundamental wavelengths of 805 nm and 850 nm were selected based on the electric field enhancement factors depicted in Figs. 2(c) and 2(d), which represent peak wavelengths for the grating regions aligned parallel and perpendicular to the pump beam

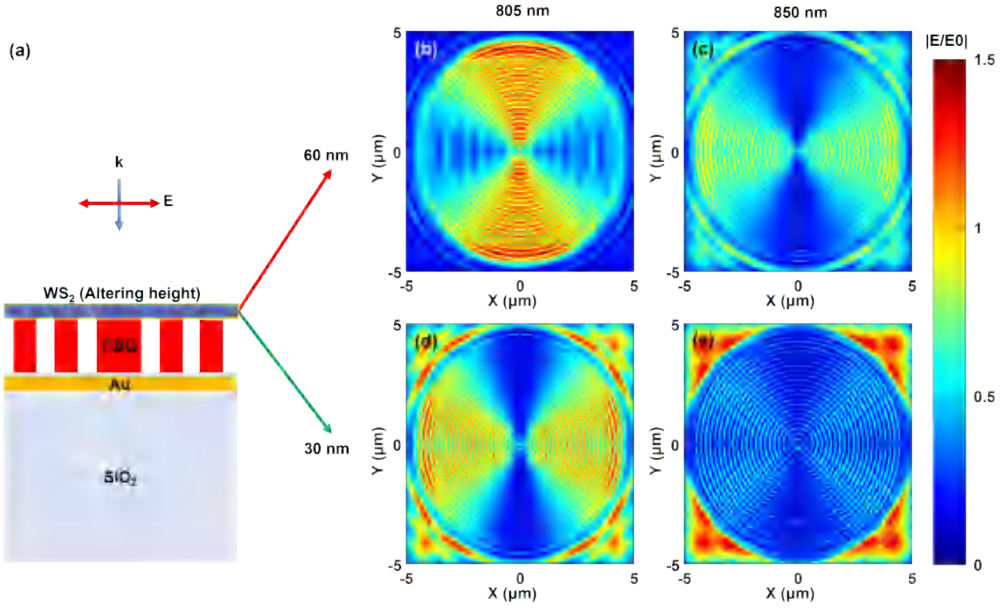

Fig. 3. (a) Schematic of the simulated multilayer WS_2-CBG/Au/SiO_2 structure, with varying WS_2 thicknesses of 60 nm and 30 nm. The red horizontal line indicates the position of the electric field detector. (b)-(d) In-plane (x-y plane) electric field distributions at the center of the multilayer WS_2 for two excitation wavelengths: 805 nm (left column) and 850 nm (right column), with 60 nm thickness (top row) and 30 nm thickness (bottom row).

Optics EXPRESS

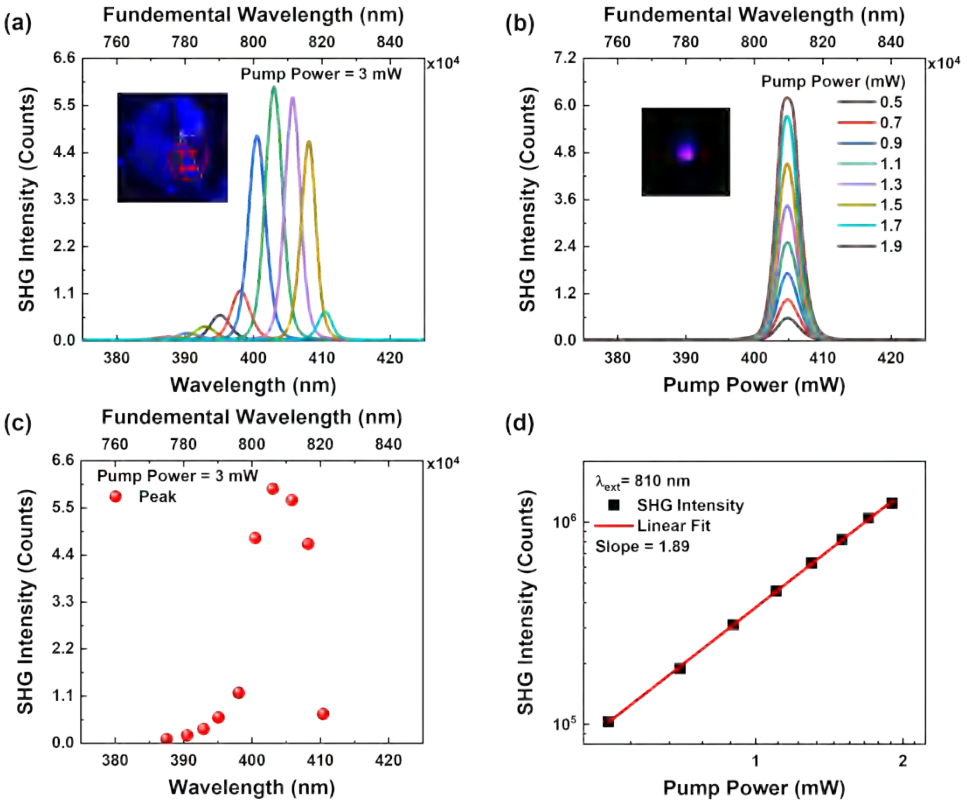

Fig. 4. (a) Second-harmonic generation (SHG) spectra of the multilayer WS_2 flake coupled with the CBG/Au/SiO_2 structure under pump wavelengths from 780 to 820 nm at 3 mW power. The SHG mapping image shows regions with excitation beams aligned parallel to the grating, indicated by red arrows. (b) Power-dependent SHG spectra of the multilayer WS_2-CBG/Au/SiO_2 structure excited by an 810 nm laser. The inset shows the SHG image obtaining from the camera. (c) Variation of peak SHG intensity as a function of excitation wavelength. (d) Log-log plot of SHG intensity versus pump power at 810 nm, illustrating the power dependence of SHG emission.

polarization. It is observed that the electric field distribution at 805 nm is enhanced in the region where the grating direction is parallel to the polarization of the pump beam, while enhancement occurs in the region where the grating direction is perpendicular to the polarization at 850 nm. Notably, the polarization of the pump beam remains consistently directed along the x-axis for both wavelengths, resulting in a wavelength-selective SHG emission pattern in the experiment that arises from the differential electric field enhancement in the WS_2 flake. For comparative analysis, the electric field distributions from the thinner 30 nm WS_2 flake are displayed in Figs. 3(d) and 3(e), revealing enhancement solely in the region where the grating is perpendicular to the pump beam polarization at 805 nm. Conversely, at 850 nm, the electric field exhibits minimal enhancement, leading to observable SHG emission in only one direction, which is consistent with the findings presented in Figs. 1(f) and 1 g. This simulation qualitatively elucidates the selective SHG emission behavior of the multilayer WS_2 flake on the CBG structure, suggesting its potential for selective nonlinear signal emission in information processing applications.

Building upon our understanding of the wavelength-selective enhancement of SHG emission from the WS_2 flake situated on the CBG structure through numerical simulations, we will further investigate the SHG spectra from an experimental standpoint. Initially, we analyze

Optics EXPRESS

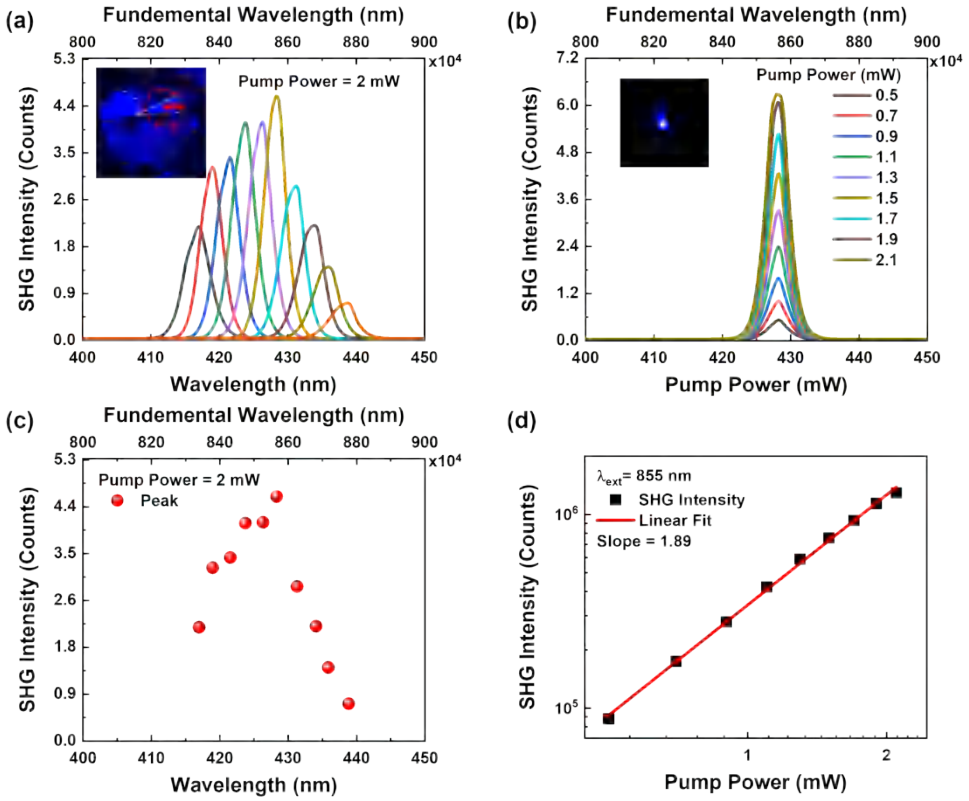

Fig. 5. (a) SHG spectra of the multilayer WS_2-CBG/Au/SiO_2 structure for pump wavelengths between 830 and 880 nm at 2 mW power, with the grating aligned perpendicular to the excitation beam's polarization. The SHG mapping image highlights regions excited with beams perpendicular to the grating, indicated by red arrows. (b) Power-dependent SHG spectra of the multilayer WS_2-CBG/Au/SiO_2 structure with excitation at 855 nm, showing the grating perpendicular to the beam's polarization. The inset shows the corresponding SHG image obtained from the camera. (c) Variation in peak SHG intensity as a function of excitation wavelength under a 2 mW pump. (d) Log-log plot showing the dependence of SHG intensity on pump power at 855 nm, illustrating the SHG response to power changes.

the scenario in which the grating region is aligned parallel to the polarization of the pump beam, with the corresponding SHG spectra presented in Fig. 4(a). The spectra reveal a peak at the SHG wavelength of 405 nm, which corresponds to a pump wavelength of 810 nm, with intensity decreasing on both sides of this wavelength, as demonstrated by the extracted SHG peak evolution illustrated in Fig. 4(c). This peak evolution is in strong agreement with the numerical simulations of electric field enhancement factor depicted in Fig. 2(d), thereby confirming the wavelength-selective enhancement enabled by the CBG structure. Furthermore, it is essential to comprehend the power dependence of the emission signal for nonlinear excitation. We maintain the pump wavelength close to the peak value, specifically, at 810 nm, to examine the power law governing SHG emission from the WS_2 flake on the CBG structure. The power-dependent SHG spectra are illustrated in Fig. 4(b), indicating that SHG intensity increases with increasing pump power, exhibiting a linear relationship within the utilized range, as corroborated in Fig. 4(d). The slope of the SHG intensity peak, derived from the linear fit, is determined to be 1.89, suggesting that signal manifesting the second-order nonlinear process in a non-saturated region.

Optics EXPRESS

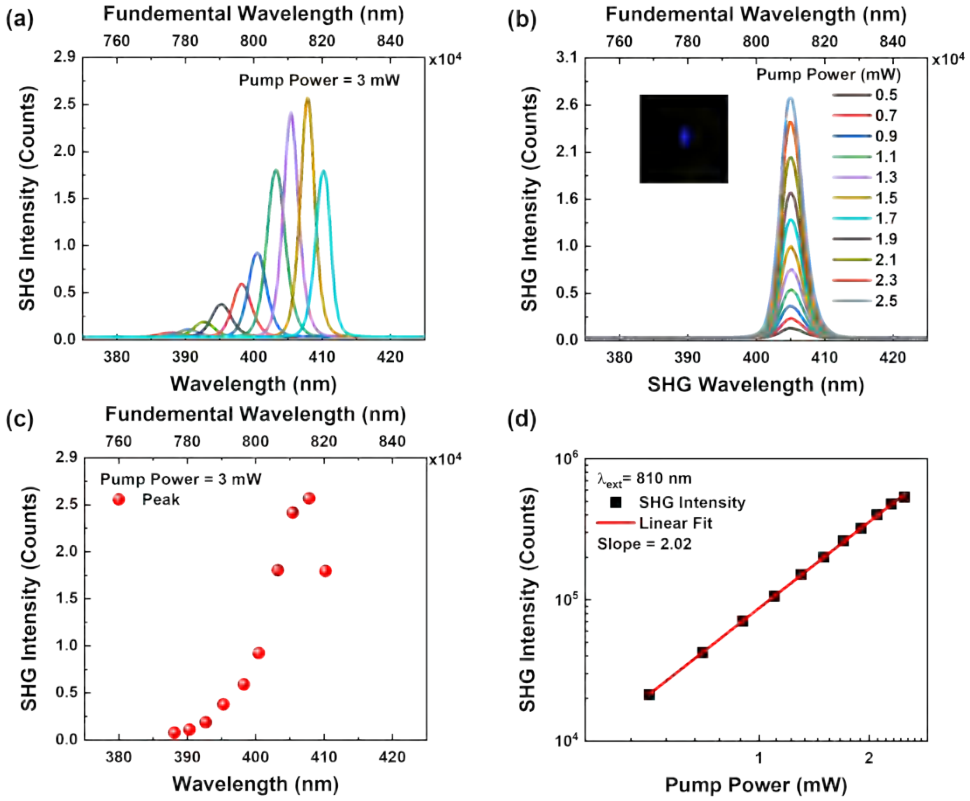

Fig. 6. (a) SHG spectra of the multilayer WS_2 on an Si/Au/SiO_2 substrate area without the CBG structure for pump wavelengths between 780 and 820 nm, with an excitation power of 3 mW. (b) Power-dependent SHG spectra of the multilayer WS_2 on an Si/Au/SiO_2 substrate area without the CBG structure under excitation from an 810 nm laser beam. The inset shows the corresponding SHG image obtained from the camera. (c) Variation in peak SHG intensity as a function of the incident beam's excitation wavelength. (d) Log-log plot of SHG intensity versus pump power at 810 nm, illustrating the relationship between SHG intensity and input power.

Conversely, Fig. 5 illustrates the SHG emission from the grating region oriented perpendicular to the polarization of the pump beam. In this configuration, the polarization of the pump beam remains consistent with that utilized in Fig. 4, while the sample is rotated by 90° to align the grating region perpendicularly to the pump beam, as illustrated in the inset of Fig. 4(a). Drawing upon insights from the numerical simulations presented in Fig. 2(c), we employed a pump beam with wavelengths ranging from 820 nm to 880 nm to investigate the pump wavelength-dependent SHG spectra of the WS_2 flake, as shown in Fig. 5(a). The results indicate a pronounced peak in the SHG spectrum at a pump wavelength of 855 nm, as demonstrated by the SHG peak evolution with respect to wavelength in Fig. 5(c), which correlates well with the numerical simulation of electric field enhancement factors depicted in Fig. 2(c). Notably, the wavelength distribution is broader than that observed in the scenario where the grating region is parallel to the pump beam polarization; the half-peak intensity spans from 830 to 860 nm in Fig. 5(c), whereas it is confined to 800 to 815 nm in Fig. 4(c). This broader distribution is attributed to the differing bandwidths of the electric field enhancement factors in the two scenarios, as indicated by the numerical results in Figs. 2(c) and (d). The power dependence of SHG emission from the WS_2 flake in the grating region oriented perpendicular to the pump beam polarization at 855 nm is

Optics EXPRESS

presented in Figs. 5(b) and (d), revealing a slope that is consistent with that observed in Fig. 4. This finding demonstrates that the CBG plays a comparable role in modifying SHG emission in the WS_2 flake, albeit at different wavelengths for the varying orientations of the grating.

In the preceding analysis, we have presented the wavelength-dependent SHG spectra of a WS_2 flake situated on a CBG structure, as illustrated in Figs. 4 and 5. Additionally, we performed comparative experiments to evaluate the SHG emission from a bare WS_2 flake placed on a $Si/Au/SiO_2$ substrate, which lacks the CBG structure, as shown in Fig. 6. The SHG spectra exhibit a peak near 815 nm in Figs. 6(a) and 6(c), which can be attributed to the intrinsic second-order nonlinear susceptibility of multilayer WS_2. The power-dependent SHG spectra at a pump wavelength of 810 nm are depicted in Fig. 6(b), where the SHG intensity increases with rising pump power. In the logarithmic plot of power versus SHG intensity presented in Fig. 6(d), the slope is calculated to be 2.02, indicating the occurrence of pure two-photon absorption in the WS_2 flake, which is consistent with our prior investigations into SHG emission from multilayer TMDCs. Furthermore, the SHG power observed in this configuration is significantly weaker than that recorded for the WS_2 flake on the CBG structure, underscoring the lack of electric field enhancement afforded by the CBG structure, in alignment with the results illustrated in Fig. 1(b).

4. Conclusions

In conclusion, we have demonstrated the ability of a WS_2-CBG/Au/SiO_2 configuration to significantly enhance and modulate SHG emission in the multilayer WS_2 flake. The extent of this enhancement is influenced by both the wavelength and the polarization alignment. Distinct regions of the grating within the CBG, oriented either parallel or perpendicular to the polarization of the pump beam, yielded peak SHG intensities at specific pump wavelengths of 805 nm and 850 nm, as supported by numerical simulations of selective electric field enhancements. Power-dependent analyses further confirmed the quadratic relationship characteristic of two-photon absorption in SHG processes. Moreover, comparative studies involving WS_2 without the CBG structure highlighted the critical role of the CBG in enabling selective control over SHG. This research underscores the potential of CBG structures to engineer nonlinear optical responses in multilayer TMDCs, indicating promising applications in photonic devices and information processing technologies. Additionally, the selectively enhanced and modified SHG emission achieved through coupling with CBG may be applicable to other van der Waals materials with strong nonlinear susceptibility, such as GaSe [40] and TMDCs exhibiting a 3R phase [14,21].

Funding. National Natural Science Foundation of China (12174123, 12374347, 92365112); Guangdong Basic and Applied Basic Research Foundation (2022A1515010747); Start-Up Funding of Guangdong Polytechnic Normal University (2022SDKYA007).

Disclosures. The authors declare no conflicts of interest.

Data availability. Data underlying the results presented in this paper are not publicly available at this time but may be obtained from the authors upon reasonable request.

References

1. P. Ho, "Twenty years of 2D materials," Nat. Phys. **20**(1), 1 (2024).
2. M. Bernardi, C. Ataca, M. Palummo, *et al.*, "Optical and electronic properties of two-dimensional layered materials," Nanophotonics **6**(2), 479–493 (2017).
3. S. Manzeli, Y.-C. Lin, D. Pasquier, *et al.*, "2D transition metal dichalcogenides," Nat. Rev. Mater. **2**(8), 1–15 (2017).
4. Y.-C. Lin, R. Torsi, R. Younas, *et al.*, "Recent advances in 2D material theory, synthesis, properties, and applications," ACS Nano **17**(11), 9694–9747 (2023).
5. Z. Xie, T. Zhao, X. Yu, *et al.*, "Nonlinear optical properties of 2D materials and their applications," Small **20**(34), 2311621 (2024).
6. X. Wen, Z. Gong, D. Li, *et al.*, "Nonlinear optics of two-dimensional transition metal dichalcogenides," InfoMat **1**(3), 317–337 (2019).
7. A. R. Khan, L. Zhang, K. Ishfaq, *et al.*, "Optical harmonic generation in 2D materials," Adv. Funct. Mater. **32**(3), 2105259 (2022).

Optics EXPRESS

8. W. Huang, Y. Xiao, F. Xia, *et al.*, "Second harmonic generation control in 2D layered materials: status and outlook," Adv. Funct. Mater. **34**(16), 2310726 (2024).
9. N. Kumar, S. Najmaei, Q. Cui, *et al.*, "Second harmonic microscopy of monolayer MoS_2," Phys. Rev. B **87**(16), 161403 (2013).
10. L. M. Malard, T. V. Alencar, A. P. M. Barboza, *et al.*, "Observation of intense second harmonic generation from MoS_2 atomic crystals," Phys. Rev. B **87**(20), 201401 (2013).
11. Y. R. Shen, *Principles of nonlinear optics* (1984).
12. Y. Li, Y. Rao, K. F. Mak, *et al.*, "Probing symmetry properties of few-layer MoS_2 and h-BN by optical second-harmonic generation," Nano Lett. **13**(7), 3329–3333 (2013).
13. Z. Wang, M. Zhao, M. Zhao, *et al.*, "Two-dimensional materials for tunable and nonlinear metaoptics," Adv. Photonics **6**(03), 034001 (2024).
14. M. Zhao, Z. Ye, R. Suzuki, *et al.*, "Atomically phase-matched second-harmonic generation in a 2D crystal," Light: Sci. Appl. **5**(8), e16131 (2016).
15. J. Zeng, M. Yuan, W. Yuan, *et al.*, "Enhanced second harmonic generation of MoS_2 layers on a thin gold film," Nanoscale **7**(32), 13547–13553 (2015).
16. J. Zeng, J. Li, H. Li, *et al.*, "Effects of substrates on the nonlinear optical responses of two-dimensional materials," Opt. Express **23**(25), 31817–31827 (2015).
17. A. Dewambrechies, A. Yu. Polyakov, B. Küçüköz, *et al.*, "Enhanced second-order nonlinearities at strained ultrasharp zigzag edges in multilayer MoS_2," J. Phys. Chem. C **127**(31), 15395–15405 (2023).
18. B. Zhou, J. H. Kang, B. Hu, *et al.*, "Giant second harmonic generation in bulk monolayer MoS_2 thin films," Matter **7**(7), 2448–2459 (2024).
19. L. Huang, A. Krasnok, A. Alú, *et al.*, "Enhanced light-matter interaction in two-dimensional transition metal dichalcogenides," Rep. Prog. Phys. **85**(4), 046401 (2022).
20. S. Busschaert, R. Reimann, M. Cavigelli, *et al.*, "Transition metal dichalcogenide resonators for second harmonic signal enhancement," ACS Photonics **7**(9), 2482–2488 (2020).
21. G. Zograf, A. Yu. Polyakov, M. Bancerek, *et al.*, "Combining ultrahigh index with exceptional nonlinearity in resonant transition metal dichalcogenide nanodisks," Nat. Photonics **18**(7), 1–7 (2024).
22. M. Panmai, J. Xiang, L. Zhou, *et al.*, "Revealing Mie resonances with enhanced and suppressed second-order nonlinear optical responses in a hexagonal-prism-like MoS_2 nanoparticle," Laser Photonics Rev. **17**(11), 2300346 (2023).
23. T. Yu, M. Panmai, S. Li, *et al.*, "Anisotropically enhanced second harmonic generation in a WS_2 nanoparticle driven by optical resonances," ACS Appl. Nano Mater. **7**(1), 726–735 (2024).
24. B. Kucukoz, B. Munkhbat, T. O. Shegai, *et al.*, "Boosting second-harmonic generation in monolayer rhenium disulfide by reversible laser patterning," ACS Photonics **9**(2), 518–526 (2022).
25. M. Nauman, J. Yan, D. de Ceglia, *et al.*, "Tunable unidirectional nonlinear emission from transition-metal-dichalcogenide metasurfaces," Nat. Commun. **12**(1), 5597 (2021).
26. N. Bernhardt, K. Koshelev, S. J.U. White, *et al.*, "Quasi-BIC resonant enhancement of second-harmonic generation in WS_2 monolayers," Nano Lett. **20**(7), 5309–5314 (2020).
27. B. Chen, Z. He, Z.-J. Liu, *et al.*, "Simultaneously enhanced linear and nonlinear photon generations from WS_2 by using dielectric circular Bragg resonators," Nanophotonics **9**(8), 2587–2592 (2020).
28. M. Davanco, M. T. Rakher, D. Schuh, *et al.*, "A circular dielectric grating for vertical extraction of single quantum dot emission," Appl. Phys. Lett. **99**(4), 1 (2011).
29. J. Liu, R. Su, Y. Wei, *et al.*, "A solid-state source of strongly entangled photon pairs with high brightness and indistinguishability," Nat. Nanotechnol. **14**(6), 586–593 (2019).
30. Z. Li, Z. Hu, X. Ye, *et al.*, "Enhanced second-harmonic generation in thin-film lithium niobate circular Bragg nanocavity," Nano Lett. **24**(37), 11676–11682 (2024).
31. Y. Hua, Y. Wei, B. Chen, *et al.*, "Directional and fast photoluminescence from $CsPbI_3$ nanocrystals coupled to dielectric circular Bragg gratings," Micromachines **12**(4), 422 (2021).
32. O. Iff, Q. Buchinger, M. Moczała-Dusanowska, *et al.*, "Purcell-enhanced single photon source based on a deterministically placed WSe_2 monolayer quantum dot in a circular Bragg grating cavity," Nano Lett. **21**(11), 4715–4720 (2021).
33. X. Zhang, W. Huang, C. De-Eknamkul, *et al.*, "Azimuthally polarized and unidirectional excitonic emission from deep subwavelength transition metal dichalcogenide annular heterostructures," ACS Photonics **8**(10), 2861–2867 (2021).
34. L. Zhou, M. Panmai, S. Li, *et al.*, "Lighting up Si nanoparticle arrays by exploiting the bound states in the continuum formed in a Si/Au hybrid nanostructure," ACS Photonics **9**(9), 2991–2999 (2022).
35. A. R. Beal and H. P. Hughes, "Kramers-Kronig analysis of the reflectivity spectra of 2H-MoS_2, 2H-$MoSe_2$ and 2H-$MoTe_2$," J. Phys. C: Solid State Phys. **12**(5), 881–890 (1979).
36. P. B. Johnson and R. W. Christy, "Optical constants of the noble metals," Phys. Rev. B **6**(12), 4370–4379 (1972).
37. E. D. Palik, *Handbook of Optical Constants of Solids* (Academic press, 1998), Vol. 3.
38. S. Viarbitskaya, A. Teulle, R. Marty, *et al.*, "Tailoring and imaging the plasmonic local density of states in crystalline nanoprisms," Nat. Mater. **12**(5), 426–432 (2013).

Optics EXPRESS

39. C. Zhang, Y. Xu, J. Liu, *et al.*, "Lighting up silicon nanoparticles with Mie resonances," Nat. Commun. **9**(1), 2964 (2018).
40. Z. Liu, J. Wang, B. Chen, *et al.*, "Giant enhancement of continuous wave second harmonic generation from few-layer GaSe coupled to high-Q quasi bound states in the continuum," Nano Lett. **21**(17), 7405–7410 (2021).